Trilayer dissolving polymeric microneedle array loading Rose Bengal transfersomes as a novel adjuvant in early-stage cutaneous melanoma management

Sara Demartis [a,b], Qonita Kurnia Anjani [b], Fabiana Volpe-Zanutto [b], Alejandro J. Paredes [b], Subrin A. Jahan [b], Lalitkumar K. Vora [b], Ryan F. Donnelly [b,*], Elisabetta Gavini [c]

[a] Department of Chemical, Physical, Mathematical and Natural Sciences, University of Sassari, Italy
[b] School of Pharmacy, Queen's University Belfast, Belfast, UK
[c] Department of Medicine, Surgery and Pharmacy, University of Sassari, Sassari, Italy

ARTICLE INFO

ABSTRACT

Melanoma remains a global concern, but current therapies present critical limitations pointing out the urgent need for novel strategies. Among these, the cutaneous delivery of drugs selectively damaging cancer cells is highly attractive. Rose Bengal (RB) is a dye exhibiting selective cytotoxicity towards melanoma, but the high water solubility and low permeability hinder its therapeutic potential. We previously developed RB-loaded transfersomes (RBTF) to mediate the RB dermal delivery; however, a platform efficiently delivering RBTF in the deepest strata is essential for a successful therapeutic activity. In this regard, dissolving microneedles release the encapsulated cargo up to the dermis, painlessly piercing the outmost skin layers. Therefore, herein we developed and characterised a trilayer dissolving microneedle array (RBTF-TDMNs) loading RBTF to maximise RBTF intradermal delivery in melanoma management. RBTF-TDMNs were proven strong enough to pierce excised porcine skin and rapidly dissolve and deposit RBTF intradermally while maintaining their physico-chemical properties. Also, 3D visualisation of the system itself and while penetrating the skin was performed by multi-photon microscopy. Finally, a dermatokinetic study showed that RBTF-TDMNs offered unique delivery efficiency advantages compared to RBTF dispersion and free drug-loaded TDMNs. The proposed RBTF-TDMNs represent a valuable potential adjuvant tool for the topical management of melanoma.

1. Introduction

Cutaneous melanoma is one of the most aggressive forms of skin cancer and one of the leading causes of cancer-related mortality due to its metastatic power. From 1990 to 2019, the incidence of melanoma increased by 170% to 289,950 and death increased by 90% to 62,840 globally (Li et al., 2022). Most patients with newly diagnosed melanoma suffer from an early-stage disease still localised to the skin. The majority of those cases have a good prognosis and are usually treated by the surgical excision, which removes the primary tumour with adequate margins to ensure the best chances of long-term survival (Leonardi et al.,

2018; Newcomer et al., 2022). The historically supported surgical margins to minimise the possibility of late recurrence are 5 cm, measured from the edge of the lesion during surgery. However, removing such a wide tissue section is not convenient when the disease affects anatomical locations such as hands, feet, head, neck and the anogenital area. Indeed, apart from aesthetic disfiguring, this procedure implies a complex reconstruction, long-term recovery and temporal disability, with increased morbidity in the previously mentioned anatomical area (Leonardi et al., 2018; Newcomer et al., 2022). Non-surgical therapeutic approaches include chemotherapy, immuno-therapy, radiotherapy and photodynamic therapy, along with the

---

limitations of induced resistance to immuno-chemotherapeutics or intralesional treatment and side effects generally caused by the lack of selectivity (Domingues et al., 2018). Hence, surgical resection remains the primary option; nevertheless, there is an urgent need to reduce the surgical margins to improve the patient's recovery and compliance without posing a risk of a late recurrence. Considering the localisation of melanoma at an early stage, malignant cells are easily accessible from the skin's surface, which can be potentially used as a localised delivery route for immuno-chemotherapeutics, avoiding systemic administration and related disadvantages (Cullen et al., 2020). However, the *stratum corneum* (SC) is a widely documented barrier to solute penetration, restraining topical and transdermal bioavailability of the active pharmaceutical ingredients (APIs) (Krishnan and Mitragotri, 2020; Portugal et al., 2021).

Rose Bengal (RB) is a dye mainly known for its colouring and photosensitising properties (Vanerio et al., 2019). The intrinsic cytotoxicity of RB was discovered in 1986 (Ito et al., 1986); since then, its anticancer activity has been tested, demonstrating its selective and effective tumour toxicity on melanoma, breast cancer, ovarian carcinoma, and colon and gastric cancers (Demartis et al., 2021a). *In-vitro* studies proved that RB induced death in melanoma cell lines secondary to releasing proteases, preferentially entering cell lysosomes, and sparing healthy cells (Mousavi and Hersey, 2007; Mousavi et al., 2006); Based on these outcomes, the intralesional injection of 10% Rose Bengal disodium solution (PV-10^{TM}) was tested in clinical trials to treat the metastatic disease with promising results (ClinicalTrials.gov Identifiers: NCT00521053, NCT00219843). In this regard, a study explored the intralesional injection of PV-10^{TM} in melanoma-bearing mice and elucidated a second systemic RB mechanism of action due to the onset of a tumour-specific immune response (Liu et al., 2016). In the view of managing melanoma at its early stages, a topical application of RB is undoubtedly preferable to the current invasive route of administration. Nevertheless, the most substantial challenge in delivering RB through the cutaneous way is related to its high molecular weight (1017.64 g/mol), water solubility (100 g/L) and anionic nature. These characteristics limit the RB permeation through the biological barriers, including SC, as well as the cellular uptake and, consequently, its therapeutic potential (Demartis et al., 2021a). To obviate this issue, we previously formulated RB into green and biocompatible flexible lipid nanovesicles, transfersomes (TF) (Demartis et al., 2021b). The *in-vitro* release study highlighted that RB-loaded TF (RBTF) were able to release RB in a controlled manner compared to RB aqueous solution; furthermore, the *ex-vivo* epidermis permeation study showed that RBTF significantly improved RB permeation through the epidermis. Also, the RBTF blocked the proliferation of melanoma cells *in-vitro* in a more effective way compared to the free drug in solution; hence, loading RB in TF is critical to enhancing cellular uptake and therapeutic efficiency. However, its current pharmaceutical form, a liquid dispersion, does not have the required consistency for topical application, and the RB dosage and release cannot be suitably controlled. For this purpose, semisolid or solid-like formulations are the preferred vehicles as they stay *in situ* and deliver drugs in a better-controlled manner (Walters and Brain, 2002). This scenario offers an exciting prospect to explore a novel platform that efficiently delivers RBTF while maintaining its physicochemical properties to preserve the advantages provided by nanotechnology.

For the last decades, microneedle (MN) arrays have actively been investigated as a physical enhancement of cutaneous drug delivery as they disrupt the skin barrier innovating the approach to treating skin diseases (Yang et al., 2021). Dissolving MN arrays have gained much attention for their biocompatibility, excellent biodegradability, and high loading capacity of APIs (Li et al., 2021; Paredes et al., 2021). Fabricated with soluble polymers, dissolving MNs gradually dissolve in the tissue fluid upon skin application by creating temporary aqueous microchannels, consequently releasing the encapsulated cargo in a controlled manner with precise drug dosage. The advantages of using dissolving MNs rely on a minimally invasive device that is easily self-administrable

to the skin without causing any discomfort or bleeding, exposing the deepest skin strata to the cargo depot following a one-step application (Aldawood et al., 2021; Yang et al., 2021). Considering these features, dissolving MNs have been successfully proposed to optimise the delivery of nanoparticles (NPs) into the skin (Permana et al., 2020; Ramalheiro et al., 2020). The combination of MNs and NPs technologies solves several issues, including drug solubility, stability, permeability, half-life and targeted drug delivery (Salwa et al., 2021). Notably, recent works have revealed the benefits of including liposome-like nanovesicles in dissolving MNs to sustain a wide range of biomedical applications, including cancer (Sharma et al., 2022; Yang et al., 2019; Zhou et al., 2020), dementia (Srivastava and Thakkar, 2021, 2020), vaccination (Lanza et al., 2020), osteoarthritis (Zhou et al., 2021), and psoriasis (Xi et al., 2022).

Based on the previous considerations, herein, we present an RB delivery platform consisting of RBTF loaded into a trilayer dissolving MN array (TDMNs). The use of a trilayer MN array instead of a standard one derives from the need to contrast the supposed softening effect exerted by lipid and surfactant materials; furthermore, due to the photoinstability of RB, the third layer has been added to prevent undesired drug degradation. The study aims to provide a suitable pharmaceutical form for delivering RBTF intradermally as an adjuvant tool in early-stage melanoma surgical management. In this view, the RBTF-loaded TDMNs (RBTF-TDMNs) were developed to be applied after the surgery to eradicate cancer cells that escaped the medical procedure (Napolitano et al., 2018). Following this approach, only the effective melanoma lesion would be removed, reducing the known surgical margins of 5 cm and consequently the patient's recovery without posing a risk for a late recurrence. Mainly, TDMNs were selected to provide a controlled dosage and release of RBTF beyond the SC without modifying the essential RBTF physicochemical features. Experimentally, a previous preformulation study adapted the already developed RBTF for integrating them into the polymeric matrix; then, the optimised RBTF were used to prepare the RBTF-loaded TDMNs (RBTF-TDMNs). The final array was evaluated in terms of physicochemical and mechanical properties, both *in-vitro* and *ex-vivo*. The physical stability of RBTF following the integration in RBTF-TDMNs was also assessed. Finally, a dermatokinetic study was performed using Franz diffusion cells to determine the intradermal delivery efficiency of the novel RBTF-TDMNs array.

2. Materials and methods

2.1. Materials

Rose Bengal disodium salt (RB), cholesterol, Span^{TM} 80, HPLC grade methanol, ammonium acetate, sodium hydroxide, phosphate-buffered saline (PBS) tablets (pH 7.3–7.5), poly (vinyl alcohol) (PVA) (9–10 kDa) and dimethyl sulfoxide (DMSO) were purchased by Sigma-Aldrich (St. Louis, MO). Polyvinylpyrrolidone (PVP) Plasdone^{TM} K-29/32 (58 kDa) and Plasdone^{TM} K-90 (1,570 kDa) were obtained from Ashland (Wilmington, Delaware, U.S). Lipoid S 100 was obtained by Lipoid GmbH (Ludwigshafen, Germany). Uranyl acetate (gadolinium acetate tetrahydrate) was purchased by Ted Pella Inc (Redding, CA). Ethanol (industrial methylated spirit 99.5%) was obtained by Atomic Scientific (Manchester, UK). Ultrapure water was obtained from a water purification system (Elga PURELAB DV 25, Veolia Water Systems, Dublin, Ireland). Silicone elastomer (Silastic^{TM} RTV-4250-S BASE) and curing agent (Silastic^{TM} RTV-4250-S Silicone Curing Agent) were purchased from Notcutt Ltd, Surrey, UK. Reagent A (LSR9-9508–30 Part A Silicone Elastomer) and Reagent B (LSR9-9508–30 Part B Silicone Elastomer) were purchased from Polymer Systems Technology Ltd.

2.2. Preparation and characterisation of RB-loaded TF

2.2.1. Preparation of RB-loaded TF

RB-loaded TF (RBTF) were prepared by a reverse-phase evaporation

method (REV) as already described by the same authors (Demartis et al., 2021b), with slight modifications. The lipid mixture, consisting of 142 mg of Lipoid S 100, 26 mg of cholesterol and 14 µL of Span^{TM} 80, was dissolved in 5 mL of ethanol and homogenised with 10 mL of RB aqueous solution (RB = 2 mg/mL) by a probe-type ultrasonic device (Davidson & Hardy Ltd cooperating with Fisher Scientific, Leicestershire, UK) (60 s, 50% ultrasound (US) amplitude). Following this, ethanol was removed by rotary evaporation (Rotavapor, Buchi Labortechnik, Switzerland) under vacuum at 50 °C, and the resulting dispersion was kept for 1 h at room temperature. Finally, RBTF dispersion was further submitted to six probe sonication cycles, each consisting of 10 s of 50% US amplitude followed by an interval of 20 s (Barba et al., 2014).

2.2.2. Particle size and zeta potential analysis

The particle size, polydispersity index (PDI) and zeta potential were analysed using a NanoBrook Omni particle sizer and zeta potential analyser (Brookhaven, New York, USA). Two batches of RBTF dispersion were analysed in triplicate (n=6).

Dynamic light scattering (DLS) was employed to measure the hydrodynamic size and the PDI. Before each measurement, samples were diluted with ultrapure water to ensure that the concentration was within the required range of the instrument. The analyses were performed using the following conditions: fluid refractive index 1.333; temperature 25 °C; viscosity 0.890 cP; scattering angle 90°; equilibration time 3.0 min; and sample run time 300 s.

Zeta potential was measured through the Phase Analysis Light Scattering (PALS) technique after diluting samples with ultrapure water. The analyses were performed at 25 °C, the equilibration time was 3.0 min, and the sample run time was 300 s.

2.2.3. Morphological characterisation

RBTF morphology was investigated by microscopical techniques, including transmission electron microscopy (TEM) and multi-photon microscopy.

For TEM analysis, one drop of the sample was added on top of a carbon copper grid and stained with uranyl acetate. After 20 min, samples were washed with deionised water and dried. Following this, the grids were placed on the specimen holder. Images were acquired using a Jeol JEM-1400 Transmission electron microscope (Welwyn Garden City, UK) at the acceleration voltage of 120,000 V and magnification between x1000 and x50,000. Images were visualised with a Jeol Ruby 8 MB bottom-mounted CCD camera.

Fluorescence images were collected using Leica TCS SP8 multi-photon scanning microscope (Leica Microsystems (UK) Ltd, Milton Keynes, UK) equipped with an upright DM6 microscope body and a motorised stage. Leica Application Suite X software (3.5.7.23225) was used for image acquisitions. Samples were excited with 549 nm laser lines from the Mai Tai Deep See Mode-Locked laser system (Newport-Spectra Physics, UK). Fluorescence emission was collected *via* HyD GaAsP-spectral detectors for Rose Bengal dye between 557 nm and 660 nm. A water immersion objective HC FLUOTAR L 25x with 0.95 Numerical Aperture or dry objectives HC PL APO 10X/0.40NA or HC PL FLUOTAR L 40X0.60NA were used for image acquisition as appropriate. Fluorescence images were collected at 1024x1024 pixel resolution format and a scanner speed of 400 Hz. Image analysis was performed using the Leica Application Suite X software (3.7.020979).

2.2.4. Evaluation of RB content in RBTF dispersion

To determine RB content in RBTF dispersion, RBTF vesicles were disrupted by dissolving the dispersion in methanol with the help of a thermomixer (Eppendorf ThermoMixer^{TM} F1.5, Hamburg, Germany) set at 56° C for 20 min at 1,5000 rpm. RB amount was then quantified by UV–Vis spectrophotometry (BMG LABTECH Ltd, Bucks, UK) and calculated using the calibration curve prepared in methanol (standard solution in the range of 1–12 µg mL^{-1}; y = 0.092x + 0.0159; R^2 = 0.9997). Finally, the drug content (DC%) was determined by the following equation:

$$DC\% = \frac{RB\ quantified\ in\ RBTF\ dispersion}{Theoretical\ amount\ of\ RB\ used} \times 100 \qquad (1)$$

Three batches of RBTF were analysed in triplicate ($n = 9$).

2.3. Fabrication and morphology of RBTF-loaded TDMNs

A mould-casting technique was employed to obtain the RBTF-loaded TDMNs (RBTF-TDMNs) (Li et al., 2021; Paredes et al., 2021). The fabrication process is illustrated in Fig. 1.

The primary mould was obtained by pouring silicone elastomers into a preformed master mould and left to solidify overnight at room temperature (r.t.). The following day, a micro-mould (600 pyramidal needles of 750 µm height on a 0.76 cm^2 area) was stuck on the primary mould using silicone elastomers and dried at 80 °C for 20 min, obtaining the final mould (Ramöller et al., 2020).

A previous preformulation study identified the most suitable composition of the first layer, which is the one loading the TF (supplementary material). To prepare the first layer, the RBTF dispersion was concentrated up to 1 mL removing the water by rotary evaporation at 50° C under vacuum. Then, the RBTF dispersion was mixed with an equal portion of an aqueous polymer blend (Srivastava and Thakkar, 2020) made of 40% w/w of PVA and Plasdone^{TM} K-29/32 (1:1 ratio) in a DAC 150 FVZ SpeedMixer^{TM} (High Wycombe, England) (3,500 rpm, 3 min). The resulting formulation was poured in excess on the top of the final mould and pressed into the needle cavities using a positive pressure chamber (Protima®, TUV Rheinland, Aliquippa, PA, US) (5 bar, 4 min). Then, the excess of the formulation was carefully removed with a spatula, and the mould was placed in the pressure chamber (5 bar) for 30 min; the first layer was finally allowed to dry at r.t.. Afterwards, a ring insert was attached to the silicone mould using PVA 40% w/w as glue, and the second layer (RBTF-free), consisting of 300 µL of Plasdone^{TM} K-90 30% w/w in water, was cast and centrifuged at 5,000 rpm for 4 min followed by the immediate removal of the holder ring. After drying at r.t., the third layer, the baseplate (BP), was applied. The BP was round, with a diameter of 13 mm and a thickness of 0.6 mm; it was 3D-printed using an Ultimaker 3 (Ultimaker B.V., Geldermalsen, The Netherlands) with a 0.4 mm extruder nozzle loaded with PLA filament. The BP was first attached to 3 M Microfoam^{TM} tape and then adhered to the needle base using double-sided tape. Finally, RBTF-TDMNs were carefully peeled off from the mould. Free drug-loaded TDMNs (RB-TDMNs) were prepared following the same procedure but using 1 mL of RB aqueous solution (RB=20 mg) instead of the RBTF dispersion to prepare the first layer.

To evaluate the morphological properties, RBTF-TDMNs and RB-TDMNs were visually examined by optical microscopy using a Leica EZ4W stereomicroscope (Leica Microsystems, Milton Keynes, UK), and the multi-photon microscopy as previously described in section 2.2.4.

2.4. Determination of RB content in RB-TDMNs and RBTF-TDMNs

RB amount localised to the needle area of RB-TDMNs and RBTF-TDMNs was evaluated. Briefly, BP was first detached from the TDMNs. The array area containing the MNs, including the second layer where the needle tips were held, was carefully isolated using scissors, added to 5 mL of methanol, and magnetically stirred until the complete disruption (about 30 min). Then, 1 mL was taken and centrifuged for 15 min at 14,000 rpm (Sigma Laborzentrifugen GmbH, Osterode am Harz, Germany) to precipitate the polymer. The supernatant was separated and further mixed with the help of a thermomixer set at 56 °C for 20 min to ensure the complete RB extraction. Finally, RB analysis was carried out by HPLC coupled with a fluorescence detector (FLD) (Agilent Technologies 1220 Infinity UK Ltd, Stockport, UK). The chromatographic column employed was a C18 Phenomenex SphereClone™ column ODS (1) (150 × 4.6 mm i.d. with 5 µm particle size) (Phenomenex Cheshire, UK).
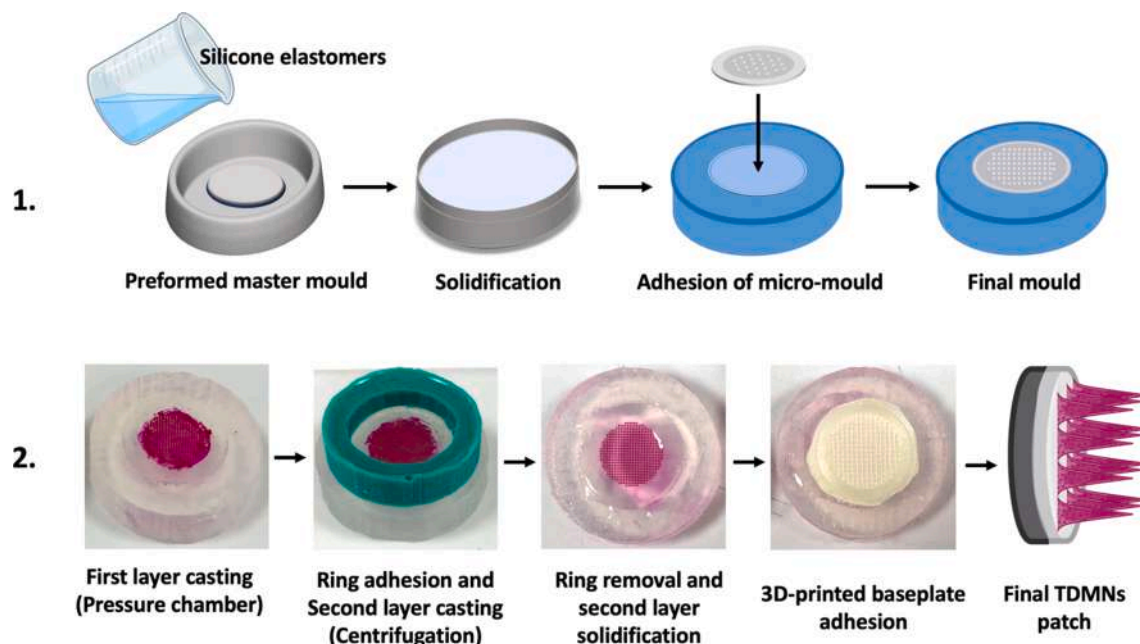
Fig. 1. **Schematic illustration of the fabrication process of RB-TDMNs and RBTF-TDMNs**. **1.1** Fabrication of the mould. **1.2** Preparation of TDMNs.

The mobile phase was a mixture of methanol and ammonium acetate buffer pH 8 (60:40 v/v), with a 1 mL/min flow rate. The excitation and emission wavelength were set at 556 nm and 573 nm, respectively, the injection volume was 40 μL, and the run time was 6 min.

Four RB-TDMNs and RBTF-TDMNs were separately analysed ($n=4$).

2.5. Physical stability of RBTF in RBTF-TDMNs

The physical stability of RBTF in RBTF-TDMNs was determined by analysing the main characteristics of the nanovesicles following the integration process in the RBTF-TDMNs. The RBTF-TDMNs were added to 5 mL of ultrapure water to dissolve the polymer and redisperse RBTF completely. The redispersed RBTF (red-RBTF) were evaluated in size, PDI, zeta potential value, and morphology, as described in subsections

2.2.2 and 2.2.3. Results of red-RBTF were compared to the original RBTF. Three RBTF-TDMNs were separately analysed three times ($n=9$).

2.6. In-vitro and ex-vivo mechanical properties testing of RB-TDMNs and RBTF-TDMNs

Mechanical strength and insertion capability were evaluated using a TA.XT2 Texture Analyser (Stable Micro Systems., Ltd., Haslemere, UK) as illustrated in Fig. 2.

The TDMNs were attached to the probe of the texture analyser, and the MNs pressed vertically against a flat aluminium surface, applying a force of 32 N for 30 s at a speed of 1.19 mm/s. These conditions simulate the average human force applied during MN array administration (Larrañeta et al., 2014). The ability of TDMNs to withstand the
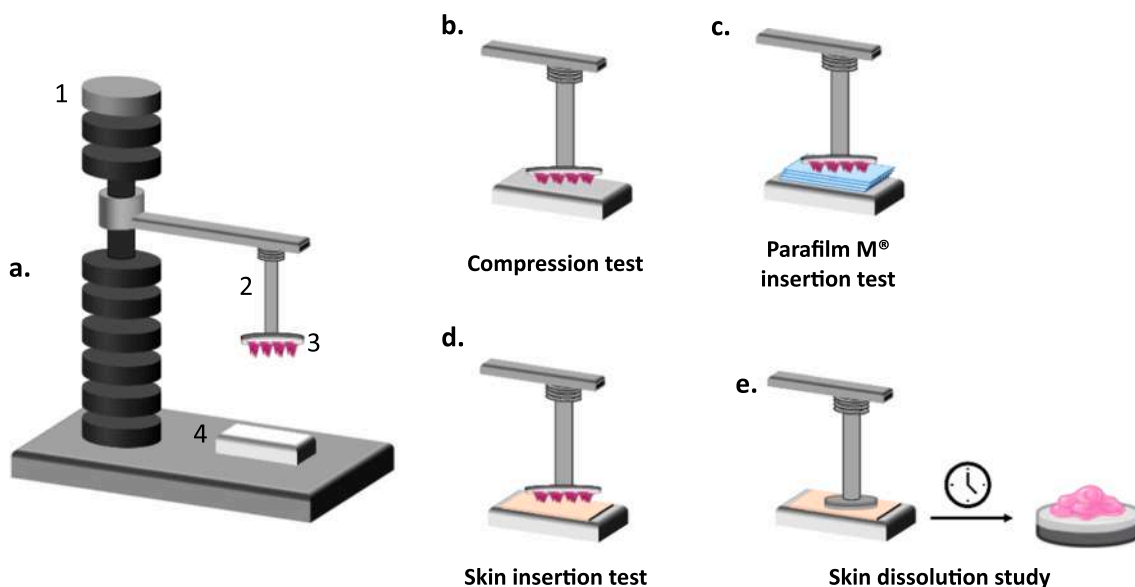

Fig. 2. **Mechanical properties testing of TDMNs. a)** Diagram of TA.XT2 Texture Analyser. 1. Texture analyser; 2. Movable aluminium probe; 3. TDMNs patch; 4. aluminium block. **b)** Testing of TDMNs' ability to withstand the compression. **c)** Insertion in Parafilm M™ skin simulant model. **d)** Insertion capability in full-thickness porcine skin. **e)** Study of the TDMNs dissolution time in full-thickness porcine skin.

compression was expressed in terms of percentage height reduction (HR %), calculated according to the equation:

$$HR\% = \frac{H_a - H_b}{H_a} x 100 \qquad (2)$$

Where H_a is the height of the MNs before the compression test, and H_b is the height of the MNs after the compression test. Three RBTF-TDMNs and three RB-TDMNs were separately evaluated; precisely, 24 MNs of each TDMNs were analysed (n=72).

Insertion capability was evaluated using the same experimental set-up. The *in-vitro* insertion study was performed by pressing the MNs against a skin simulant Parafilm M™ model described by Larrañeta and colleagues (Larrañeta et al., 2014) and widely used in the literature. The Parafilm M™ (Bemis Company Inc., Soigneis, Belgium) was cut to form eight layers stacked one on top of the other with a thickness of 1 mm (approximately 0.125 mm per layer) (Larrañeta et al., 2014; Li et al., 2021). The insertion was expressed in the number of perforations in each Parafilm M™ layer, determined under a Leica EZ4W stereomicroscope using two polarised filters (Paredes et al., 2021). Three RBTF-TDMNs and three RB-TDMNs were separately evaluated (n=3).

The insertion capability of the TDMNs was tested *ex-vivo* using the full-thickness neonatal porcine skin. First, the skin was obtained from stillborn piglets, kindly donated by the Agri-Food and Bioscience Institute (Hillsborough, Northern Ireland, UK); piglets were immediately frozen after birth at -20° C and defrosted overnight before use. Full-thickness skin was excised using a surgical scalpel and carefully shaved using a disposable razor (Gillette Blue II™, Gillette, Reading, UK). The skin was allowed to equilibrate for 30 min in PBS pH 7.4 before the experiment. The Texture Analyser was employed to perform the experiment, using the same set-up above described. The insertion depth was evaluated by multi-photon microscopy, as described in section 2.2.4.

2.7. Ex-vivo skin dissolution study

To evaluate the dissolution time, RB-TDMNs and RBTF-TDMNs were pressed against the skin, previously prepared as reported in section 2.6, and then removed at different time points (1 min, 3 min, 5 min, 10 min) (Fig. 2). The TDMNs were morphologically evaluated at each time point using a Leica EZ4 D stereo microscope.

2.8. Ex-vivo dermatokinetic study

The dermatokinetic profile of RB-TDMNs, RBTF-TDMNs and RBTF dispersion was evaluated *ex-vivo* across full-thickness neonatal porcine skin. The skin was obtained and prepared as previously described in section 2.6. The experiment was performed using Franz diffusion cells (Permergear, Hellertown, PA, USA) with a 1.77 cm² orifice area and 12 mL receptor volume. The receiver compartment was filled with 12 mL of degassed PBS pH 7.4 as the receiver medium. Meanwhile, the skin was fixed on the donor compartment with the help of ethyl 2-cyanoacrylate glue (Gorilla Glue Europe Ltd, Chorley, UK), with the SC side facing the donor compartment.

RB-TDMNs and RBTF-TDMNs were separately inserted into the full-thickness neonatal porcine skin using the manual force of the same operator for 30 s. Then, the donor chamber was carefully allocated on the top of the receiver compartment, with the inner side facing PBS. A cylindrical stainless-steel weight (5 g) was placed upon the inserted TDMNs to avoid movement or ejection. In the case of RBTF dispersion, the formulation was added onto the skin surface within the donor compartment (0.1 mL, 100 μg of RB), already mounted on the top of the receiver compartment. The system's temperature was set at 37 ± 1 °C, and an equilibration time of 30 min was allowed before starting the experiment. The donor and the sampling ports were sealed using Parafilm M™ to minimise evaporation and contamination; the magnetic stirrers were set at 600 rpm to homogenise the receiver medium. The skin samples collected at each predetermined time point (1 h, 3 h, 6 h, 12 h, 24 h) were carefully cleaned and placed on a hot plate for 2–3 min at 60 °C to separate the epidermis from the dermis. To extract RB from the skin samples, 0.5 mL of distilled water was added to the samples and disrupted at 50 Hz for 15 min by a Qiagen TissueLyser™ LT (UK Quiagen Ltd, Manchester, UK). Subsequently, 1 mL of DMSO was added, and the samples were further homogenised for 15 min (50 Hz); this step was repeated twice to ensure the total RB extraction from the skin. Following a centrifugation process (14,000 rpm, 15 min), the amount of RB in the supernatant was determined using HPLC (section 2.4). Three RBTF-TDMNs, RB-TDMNs and RBTF dispersion, were separately analysed (n=3).

2.9. Statistical analysis

All data in this study were presented as means ± standard deviation (SD) of the mean and were calculated using GraphPad Prism™ version 9.3.1 (GraphPad Software, San Diego, California, USA). The same software was used to determine statistical differences by Student's *t*-test and analysis of variance (ANOVA). A value of $p < 0.05$ was noted as statistically significant.

3. Results and discussion

3.1. Preparation and characterisation of RBTF

Before the integration of RB in the TDMNs, RB was formulated in TF by a reverse-phase evaporation technique, as described in our previous work (Demartis et al., 2021b). A preformulation study, detailed in the supplementary material, was performed on blank TF to evaluate if the original formulation was suitable for the integration into the polymeric matrix of PVA and PVP. Results revealed that the initial lipid concentration (Lipoid S100 and cholesterol, 47.5 mg/mL) was excessive, hampering the proper MNs formation. Therefore, we decreased the lipid concentration to 16.88 mg/mL, leading to MNs with promising morphological (Fig. S1, supplementary material) and mechanical properties (Fig. S2, supplementary material). Herein denoted as RBTF, the new formulation was developed, maintaining the ratio between Lipoid S100, Span™ 80 and cholesterol unchanged compared to the original formulation.

The size of RBTF measured 62.91 ± 6.28 nm with a PDI of 0.271 ± 0.045, and the zeta potential was −38.47 ± 0.20 mV. DLS analyses indicated a dispersion in the nano-sized range, suitable to be included in dissolving MNs (Srivastava and Thakkar, 2020; Yang et al., 2019; Zhou et al., 2021). The PDI value was lower than 0.3 and the zeta potential higher than |30| mV, predicting the thermodynamic stability of the formulation (Leonyza and Surini, 2019; Permana et al., 2020). Herein, no dimensional stability test overtime of RBTF has been performed; nevertheless, the PDI and zeta potential results were in line with those presented in our initial work (Demartis et al., 2021b), where the formulations proved to be dimensionally stable over 60 days. Furthermore, NPs instability is characteristic of NPs dispersed in a liquid vehicle, where aggregation is more likely to occur. This phenomenon can be easily prevented by solvent removal and conversion into a solid-like dosage form, such as TDMNs (McGuckin et al., 2022; Permana et al., 2020; Van Eerdenbrugh et al., 2008).

TEM micrographs (Fig. 3. a, b, c) showed spherical-shaped particles. The analyses confirmed the proper formation of RBTF since the phospholipid bilayer, the primary indication of a successful liposome-like structure, is clear and easily identifiable. Considering the size lower than 100 nm and TEM evaluations, RBTF are defined as small unilamellar vesicles (SUV) (Lin et al., 2012). However, it is essential to note that DLS reports an overall average diameter of the dispersed RBTF. In conjunction with the PDI value and TEM micrographs, the presence of vesicles larger and smaller than 100 nm is highly probable.

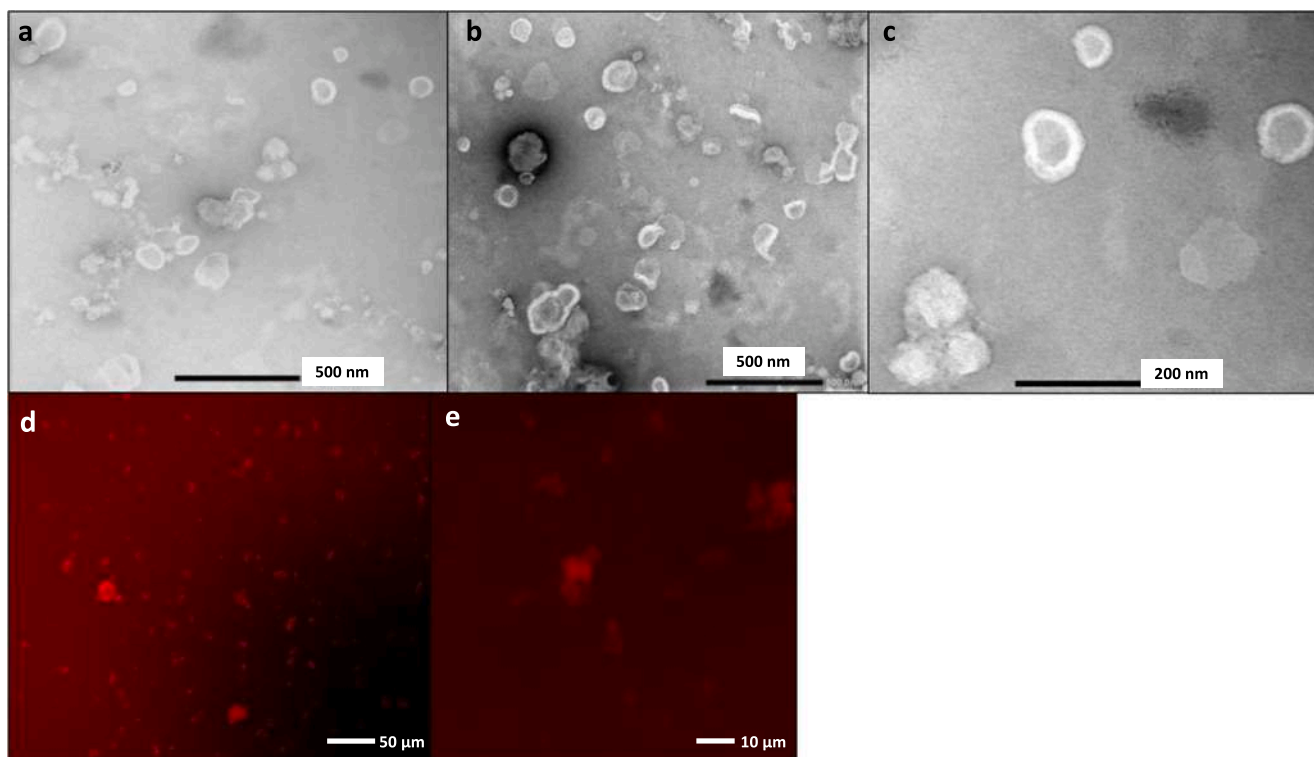Finally, the RB content in RBTF was 110.31 ± 3.49%. It is important

Fig. 3. Morphological evaluation of RBTF. a, b). TEM micrographs, 500 nm scale bar, magnification x20K; **c.** TEM micrograph, 200 nm scale bar, magnification x80K. **d, e).** Multi-photon micrographs, scale bar 50 μm and 10 μm, respectively.

to cite that the term "RBTF" refers to RB-loaded nanovesicles dispersed in the water phase; hence, the RB content is intended in the whole dispersion made of the nanovesicles and their dispersing vehicle. Herein, no physical isolation of nanovesicles was performed. This assay evaluated the chemical stability of the drug through the manufacturing process and revealed that no degradation phenomena occurred. RB has a high affinity for lipids and undoubtedly interacted with the lipid phase of the RBTF, as also proved by the negative zeta potential value (Chang et al., 2008; Demartis et al., 2021b; Hugo et al., 2011; Lee et al., 2021).

3.2. Fabrication and morphological characterisation of RB-TDMNs and RBTF-TDMNs

In this study, a trilayer dissolving MN array was proposed to sustain the intradermal delivery of RBTF. The morphology of RB-TDMNs and RBTF-TDMNs was first investigated through optical microscopy (Fig. 4, a-e). To better characterise the new RB delivery platform, a 3D reconstruction of the TDMNs via multi-photon fluorescence microscopy has been carried out; herein, the view from different perspectives is proposed (Fig. 4, f-i).

RBTF-TDMNs and RB-TDMNs were visually identical; the morphological characterisation demonstrated the successful formation of the 600 micro projections pyramidal-shaped, bubble-free, sharp, and uniformly distributed on the patch area. To reduce the drug waste, the pharmaceutical cargo was loaded only in the first layer of the TDMNs, formulated using an aqueous blend of low molecular weight PVA and PVP. It is known in the literature that the combination of these polymers forms tips with better mechanical performance than a single polymer due to the formation of hydrogen bonds amongst C=O groups of PVP and –OH groups of PVA (Salwa et al., 2021). Accordingly, in the pre-formulation study reported in the supplementary material, the combined PVA/PVP showed the best penetrability (Fig. S2, supplementary material). The first layer's formulation was forced to fill the cavities of the micro-mould by applying positive pressure, followed by water evaporation and the application of the viscous second layer by

centrifugation in the presence of a ring insert. This method allowed the formation of the entire MNs and, in the meantime, assured an excellent adhesion between the two layers (Paredes et al., 2021). Finally, as the third layer, the PLA 3D-BP was attached. The 3D-BP is expected to maximise the system's overall efficiency, thus minimising the supposed softening effect caused by the semi-solid Lipoid S100 and Span^{TM} 80; furthermore, PLA was reported to provide added mechanical strength to the MNs (Salwa et al., 2021), the pyramidal geometry of the tips was selected for the same reason (Li et al., 2021; Salwa et al., 2021). Moreover, considering that the cutaneous route is exposed to light, the use of a non-transparent 3D-BP acts as a barrier protecting RB from photodegradation.

3.3. Evaluation of RB content in RB-TDMNs and RBTF-TDMNs

Results showed that 139.31 ± 22.16 μg were loaded in RB-TDMNs, and 64.37 ± 8.61 μg in RBTF-TDMNs (p value < 0.001). No degradation processes occurred during the preparation of RBTF (section 3.1), and the two TDMNs were prepared following the same procedure. The lower RB amount in RBTF-TDMNs compared to RB-TDMNs can be attributed to a higher viscosity of the final polymer blend incorporating the mix of lipid and surfactant constituting RBTF (first layer), which may result in a greater resistance in filling the micro-mould, which is responsible for the drug loading. This phenomenon has already been observed in the literature and is more common in the case of drugs with a physical–chemical profile similar to RB (Anjani et al., 2022). The RB amount localised to the MNs area was calculated once the system was entirely dried; the needle tips were not separated from the thin second layer attached. Indeed, given an intradermal delivery, the residual amount of RB eventually migrating from the tips to the second layer is likely to deposit into the skin through the microchannel created by the insertion of the array and exploiting the permeation properties of the TF technology. The RB amounts mentioned above determined the drug dose of RB-TDMNs and RBTF-TDMNs, respectively, and were used for further evaluations.
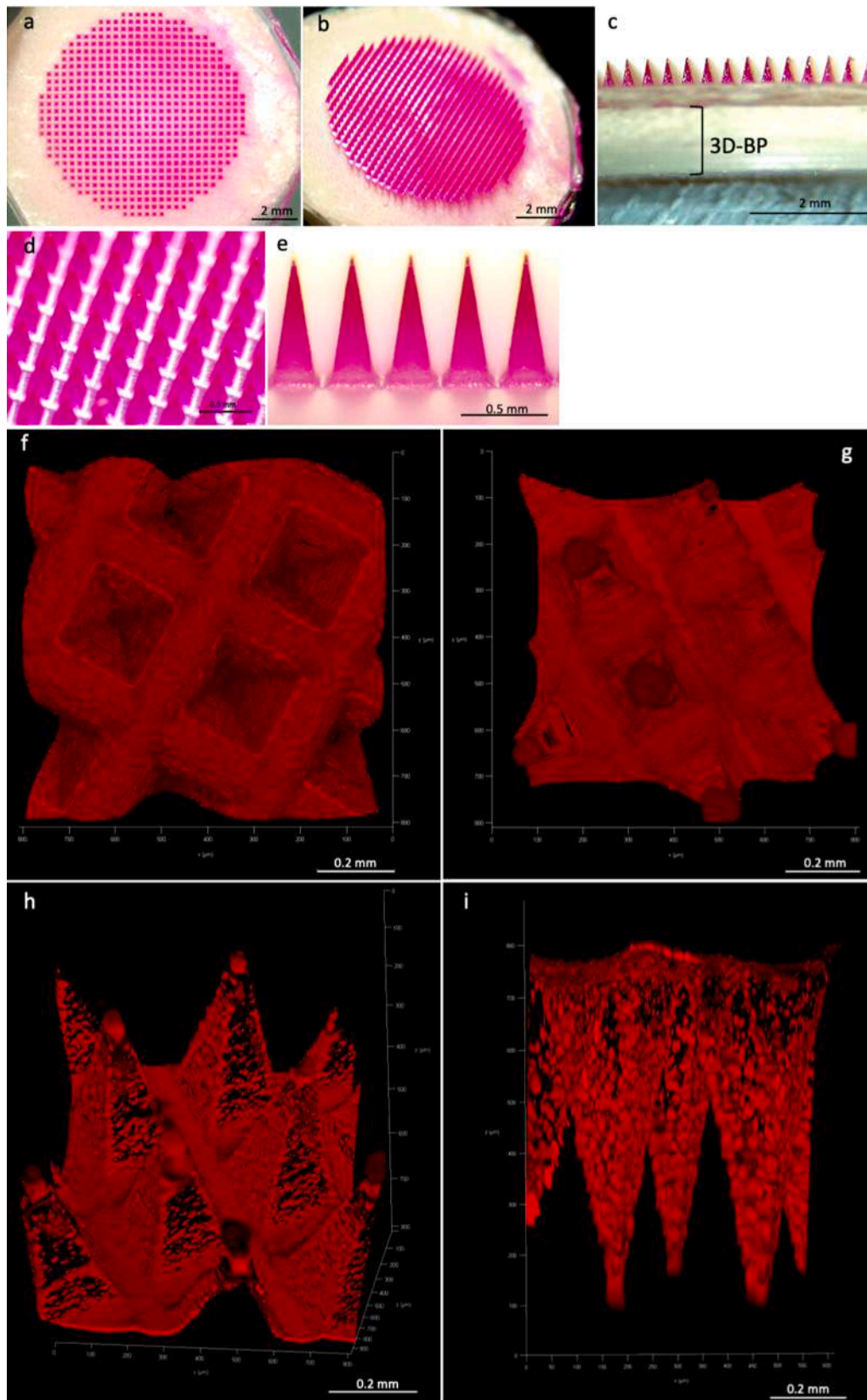
Fig. 4. Morphology of TDMNs. a-b) top view of TDMNs by optical microscopy. Scale bar 2 mm, magnification 8x. **c)** Side view, focus on trilayer TDMNs structure by optical microscopy. Scale bar 2 mm, magnification 8x. **d)** top view of TDMNs by optical microscopy. Scale bar 0.5 mm, magnification 35x. **e)** tips of TDMNs. Scale bar 0.5 mm, magnification 35x. F-i) imaging of TDMNs obtained by the 3D reconstruction by multi-photon microscopy. Scale bar 0.2 mm.

3.4. Physical stability of RBTF in RBTF-TDMNs

RBTF were integrated into TDMNs to provide a final pharmaceutical form to control the dosage, circumvent eventual stability issues and ensure the RBTF delivery to the target site. With these premises, it is essential to define the physical stability of RBTF in RBTF-TDMNs. Hence, RBTF-TDMNs were dissolved in water and then redispersed RBTF (Red-RBTF) were evaluated. Red-RBTF measured 183.62 ± 29.26 nm with a PDI of 0.224 ± 0.064 and a zeta potential value of -38.19 ± 0.14 mV. As already observed in similar investigations (Yang et al., 2019; Zhou et al., 2021), particle size significantly increased compared to the original RBTF (p value < 0.001), whereas PDI and zeta potential values did not statistically differ. TEM investigation proved that red-RBTF were spherical and unilamellar (Fig. 5. a-c); no appreciable differences were seen under the multi-photon microscopy (Fig. 5. d).

As previously discussed (section 3.1), DLS provides an overall average diameter of the NPs, which can be affected by several factors (Van Eerdenbrugh et al., 2008). As demonstrated in our previous work (Demartis et al., 2021b), RB is located inside the RBTF and intercalated beneath the phospholipid bilayer. Considering the log P of RB (0.59), we cannot exclude interactions between the polymers used and the surface of the RBTF. Indeed, the interaction between RB and PVA has been already described in the literature (El-Bashir et al., 2017), and non-well-defined structures beyond Red-RBTF were seen in the TEM micrographs, which can be hypothetically referred to as polymer residues. However, the particle size recorded is in line with the one observed in our previous work, which efficiently promoted RB permeation through the epidermis (Demartis et al., 2021b). The zeta potential was unchanged, indicating

that RB was still efficiently interacting with the lipid vesicles (Demartis et al., 2021b; Lee et al., 2021). TEM evaluations showed that Red-RBTF maintained the same structure as the RBTF before the integration process, which is the essential feature for the drug encapsulation and the intact RBTF delivery to the deepest skin strata (Yang et al., 2019).

3.5. In-vitro and ex-vivo mechanical properties of TDMNs

The effective penetration of the MNs into the skin is imperative to achieve the desired delivery goals. Therefore, we evaluated RBTF-TDMNs and RB-TDMNs' penetration ability and their mechanical resistance to the insertion force required. Human skin exhibits unique characteristics that vary depending on gender, race, proper physiological conditions, or other factors (Bhadale and Londhe, 2022). Consequently, the mechanical force necessary to assure an effective MNs insertion is not standard. However, a model method was proposed to provide a standard reference for testing MNs insertion and was adopted here as described in section 2.6 (Larrañeta et al., 2014). Fig. 6 reports the results of the *in-vitro* mechanical testing.

RB-TDMNs reported an MNs height reduction of $6.53 \pm 0.51\%$ following the 32 N compression force application against a flat solid aluminium surface. In contrast, RBTF-TDMNs suffered from a statistical higher reduction, reaching a value of $9.77 \pm 0.18\%$ (p value < 0.0001) (Fig. 6.a). The images acquired by optical microscopy (Fig. 6. c, d) showed that the MNs were sharp and pyramidal-shaped before the test. The height reduction was visible following the compression, and the tips appeared pressed but not crushed or bent. The insertion test in the Parafilm M™ skin simulant model proved that RBTF-TDMNs and RB-
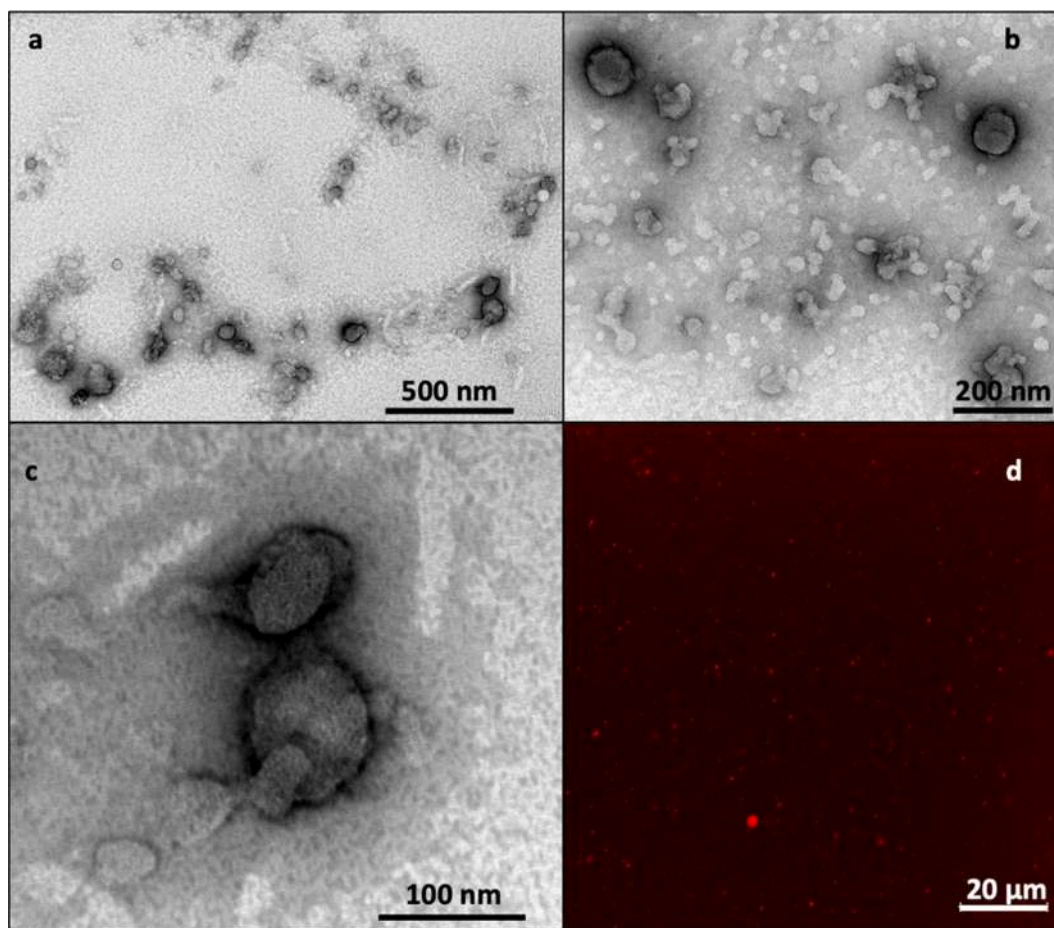

Fig. 5. Microscopical evaluation of red. RBTF. a. TEM micrographs, 500 nm scale bar, magnification x20K; **b.** TEM micrograph, 800 nm scale bar, magnification x80K; **c.** TEM micrograph, 100 nm scale bar, magnification x80K. **d.** multi-photon micrographs, scale bar 20 μm. (For interpretation of the references to colour in this figure legend, the reader is referred to the web version of this article.)
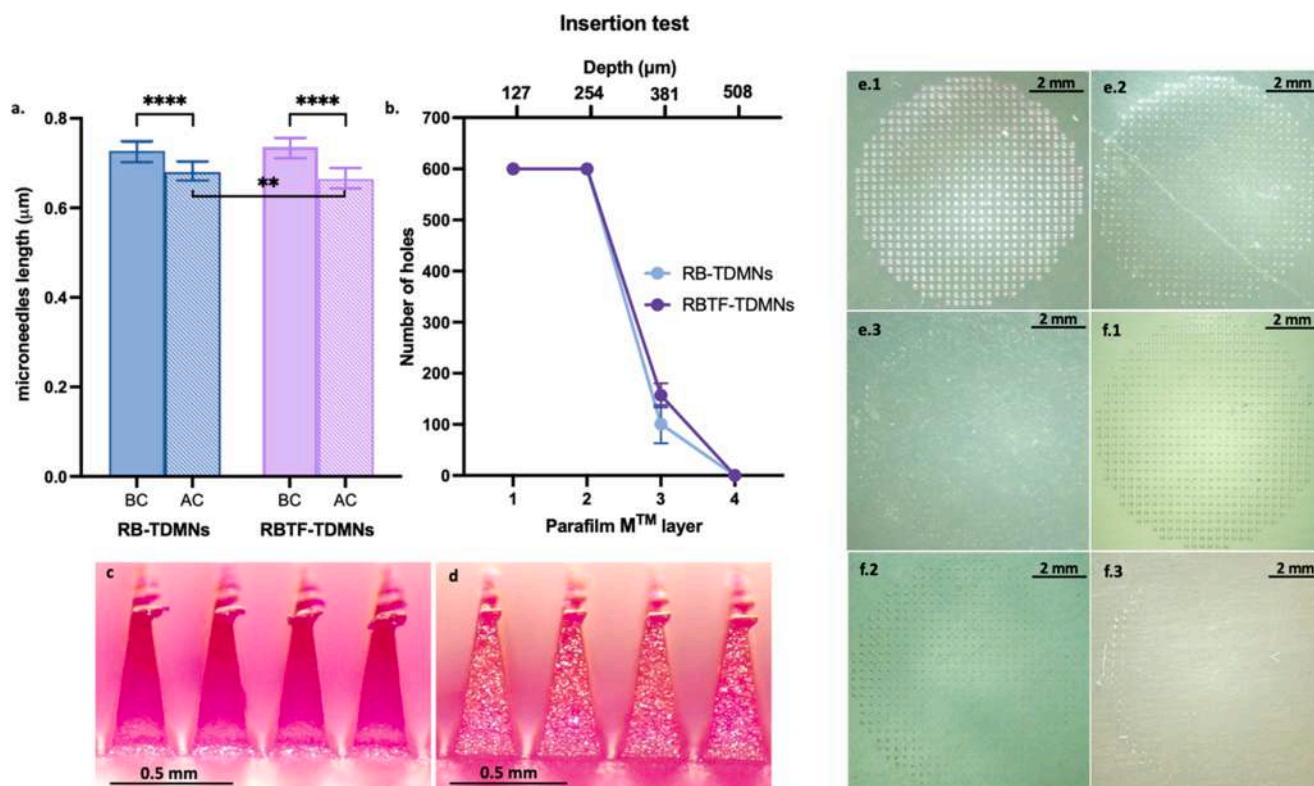
Fig. 6. *In-vitro* **mechanical testing of TDMNs. a)** MN height before and after the compression test ($n = 3$). **** p value < 0.0001; ** p value < 0.01. **b)** Insertion capability in Parafilm M^{TM} skin simulant model ($n = 3$). **c)** MNs of RBTF-TDMNs acquired with the optical microscope after the compression test. Scale bar 0.5 mm, magnification 35x **d.)** MNs of RB-TDMNs after the compression test, acquired with the optical microscope. Scale bar 0.5 mm, magnification 35x **e)** Parafilm M^{TM} sheets following the insertion of RBTF-TDMNs: first layer (e.1), the second layer (e.2), the third layer (e.3). **f)** Parafilm M^{TM} sheets following the insertion of RB-TDMNs: first layer (f.1), the second layer (f.2), and the third layer (f.3).

TDMNs entirely pierced the first two layers (Fig. 6. b, e, f), corresponding to a depth of ~ 0.254 μm. The insertion decreased in the third layer (~ 0.381 μm), creating 100–157 holes without significant differences between the two TDMNs. Even if the incorporation of lipid materials and surfactant decreased the resistance to compression, this did not appear to affect the insertion ability. Indeed, previous studies reported that an MN height reduction not above 10% and the insertion of at least two Parafilm M^{TM} layers are a prerequisite for an efficient penetration ability, and these parameters were here respected (Paredes et al., 2021; Permana et al., 2021; Volpe-Zanutto et al., 2021).

To better predict the *in-vivo* performance of RBTF-TDMNs and RB-TDMNs, we further evaluated their penetration ability *ex-vivo* in full-thickness porcine skin following the same method. In this case, the insertion was tracked under multi-photon microscopy by exploiting the fluorescence properties of RB (Wachter et al., 2002). Multi-photon fluorescence microscopy has become a very effective tool for studying skin. It provides high-resolution 3D visualisation of the analysed tissue to evaluate the accumulation and penetration properties of drugs released from cutaneous administration (Bloksgaard et al., 2013; Stracke et al., 2006). The TDMNs insertion in the skin is illustrated in Fig. 7. Briefly, Fig. 7a provide an overview of the test: Fig. 7.a1 shows only a TDMNs (red-coloured) penetrating the skin (grey-coloured) isolated by the instrument software, Fig. 7.a2 represents only the skin (grey-coloured) penetrated by the TDMNs isolated by the instrument software, and Fig. 7.a3 shows both the TDMNs and the skin. Fig. 7. b-c depicts only the TDMNs penetrating the skin, processed as Fig. 7.a3. Fig. 7.d shows the skin following the physical detachment of the RBTF-TDMNs from the skin itself; thus, it shows the residues of TDMNs remaining in the skin once they have been removed.

During the analyses, liposome-like structures were detected on the surface of RBTF-TDMNs when RBTF-TDMNs penetrated the skin (Fig. 7.

c) and were absent in the case of RB-TDMNs (Fig. 7.b). Beyond this, the multi-photon fluorescence technique confirmed the penetration ability of both the TDMNs previously anticipated by the *in-vitro* Parafilm M^{TM} insertion test. Indeed, the results from the *ex-vivo* insertion study (Fig. 7. b-c) indicated that the TDMNs could penetrate to a depth range of approximately 400–450 μm, similar to the 375 μm observed in the Parafilm M^{TM}; furthermore, the MNs structure is still recognisable into the skin following the removal of the TDMNs from the skin itself (Fig. 7. d). It was observed that the TDMNs penetration depth, both *in-vitro* and *ex-vivo*, was considerably lower than the TDMNs length, which ranges around 750 μm. The phenomenon is explained by the inherent visco-elastic properties of both Parafilm M^{TM} and skin, which resist MNs penetration, resulting in an incomplete insertion (Anjani et al., 2022). However, the thickness of the entire epidermis is approximately 83.7 ± 16.6 μm, of which 14.8 ± 4.8 μm are represented by the SC and the remaining by the viable epidermis (Sandby-Møller et al., 2003). The presented data proved that RB-TDMNs and RBTF-TDMNs could fully penetrate the epidermis, releasing the active cargo up to the dermis, de facto potentially covering the area affected by early-stage melanoma.

3.6. Ex-vivo skin dissolution study

Considering that the effective active cargo release depends on the dissolving ability of the polymeric tips, the TDMNs dissolution study following application to the skin was performed to determine the time required for complete MNs dissolution (Fig. 8) (Volpe-Zanutto et al., 2021; Zhou et al., 2021).

RBTF-TDMNs were entirely dissolved after 5 min (Fig. 8 a.3), with a bending already visible after 1 min (Fig. 8 a.1). In contrast, RB-TDMNs were wholly liquefied after 10 min, with a partial dissolution and decreased MN height after 3 min (Fig. 8 a.2). Due to the high water-
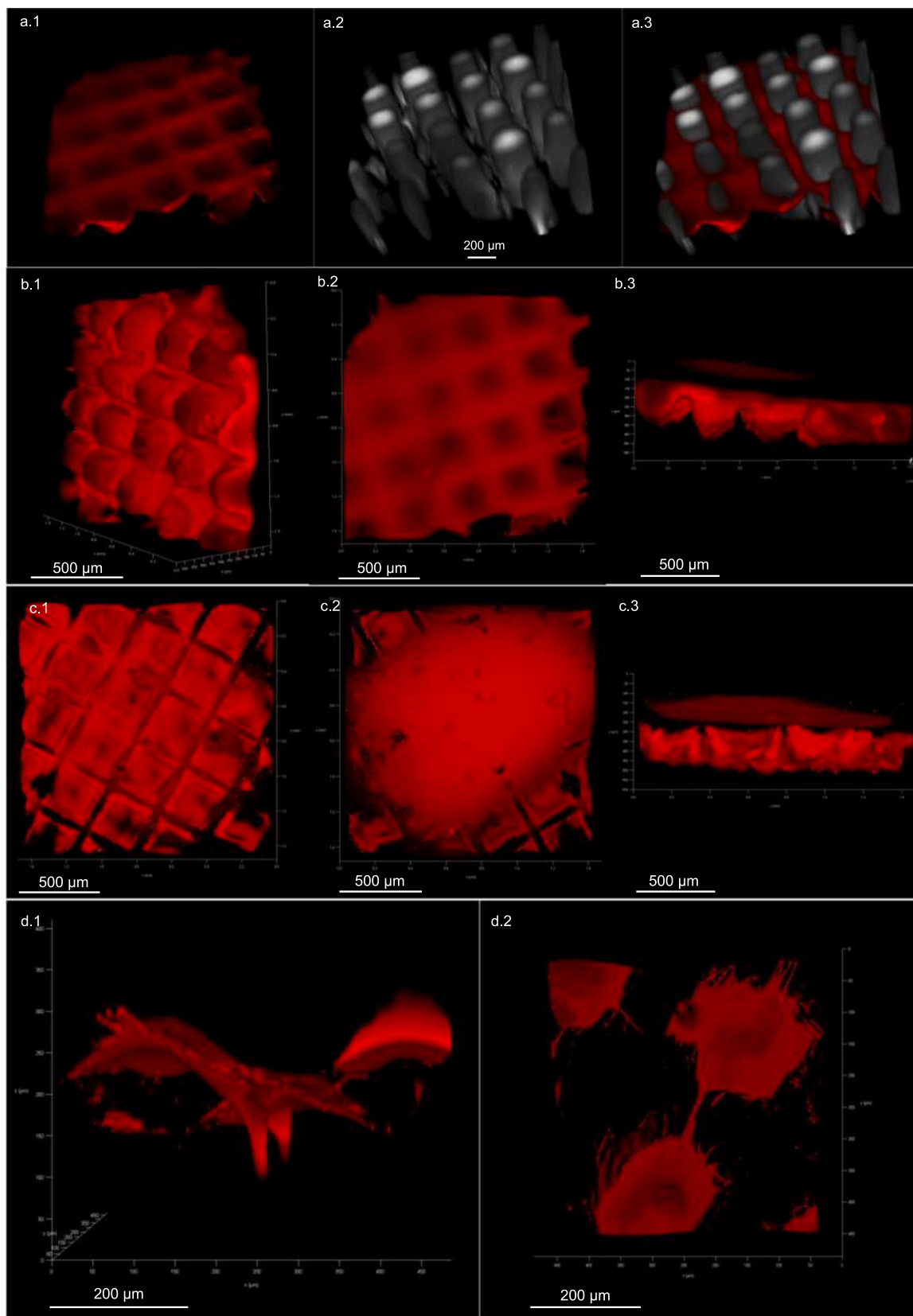
Fig. 7. 3D visualisation of the *ex vivo* TDMNs insertion in full-thickness skin by multi-photon fluorescence microscopy. a) Representation of TDMNs inserted in the skin; a.1) TDMNs inserting the skin isolated by the instrument's software; a.2) skin isolated by the instrument's software. a.3) full image of TDMNs inserted skin. Scale bar 200 µm. **b)** RB-TDMNs inserted in the skin, scale bar 500 µm; b.1) bottom-side view; b.2) top view; b.3) lateral view. **c)** RBTF-TDMNs inserted in the skin, scale bar 500 µm; b.1) bottom view; b.2).
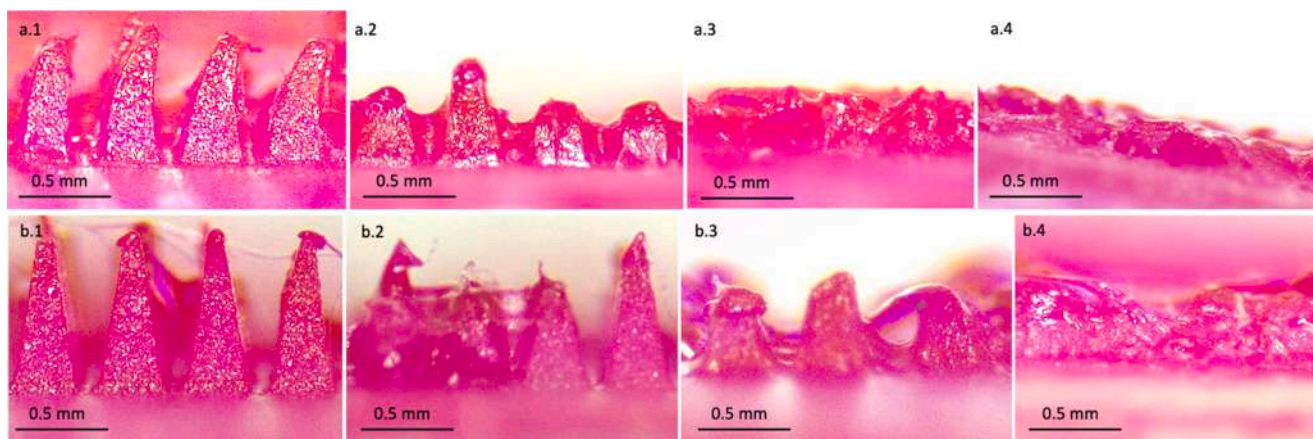
Fig. 8. *Ex-vivo* dissolution study, investigated by optical microscopy. a) Study of RBTF-TDMNs dissolution time in the skin: 1 min (a.1), 3 min (a.2), 5 min (a.3), 10 min (a.4). Scale bar 0.5 mm; magnification 35x. **b)** Study of RB-TDMNs dissolution time in the skin: 1 min (b.1), 3 min (b.2), 5 min (b.3), 10 min (b.4). Scale bar 0.5 mm; magnification 35x.

solubility of the PVA and PVP, both the TDMNs could dissolve very quickly and thoroughly. Furthermore, the presence of RBTF appeared to decrease the dissolution time of the formulation. Surfactants, represented by the Span[TM] 80, play an essential role in formulating dissolving MNs. Considering the water-rich environment characterising the dermis, it is likely that Span[TM] 80 promoted the wetting and spreading of the dermal interstitial fluid along and into the polymeric matrix, thus enhancing the water access into the MNs and finally increasing the overall dissolution rate (Anjani et al., 2022).

3.7. Ex-vivo dermatokinetic study

To assess the effectiveness of TDMNs as an RBTF delivery platform in melanoma management, we finally investigated *ex-vivo* the percutaneous absorption of RB when formulated as a transfersomal dispersion (RBTF), integrated free into TDMNs (RB-TDMNs) and incorporated as RBTF into TDMNs (RBTF-TDMNs).

RBTF-TDMNs were designed to assist the surgical management of early-stage melanoma, mainly when it affects anatomical locations where the surgical eradication is more complex and not convenient for
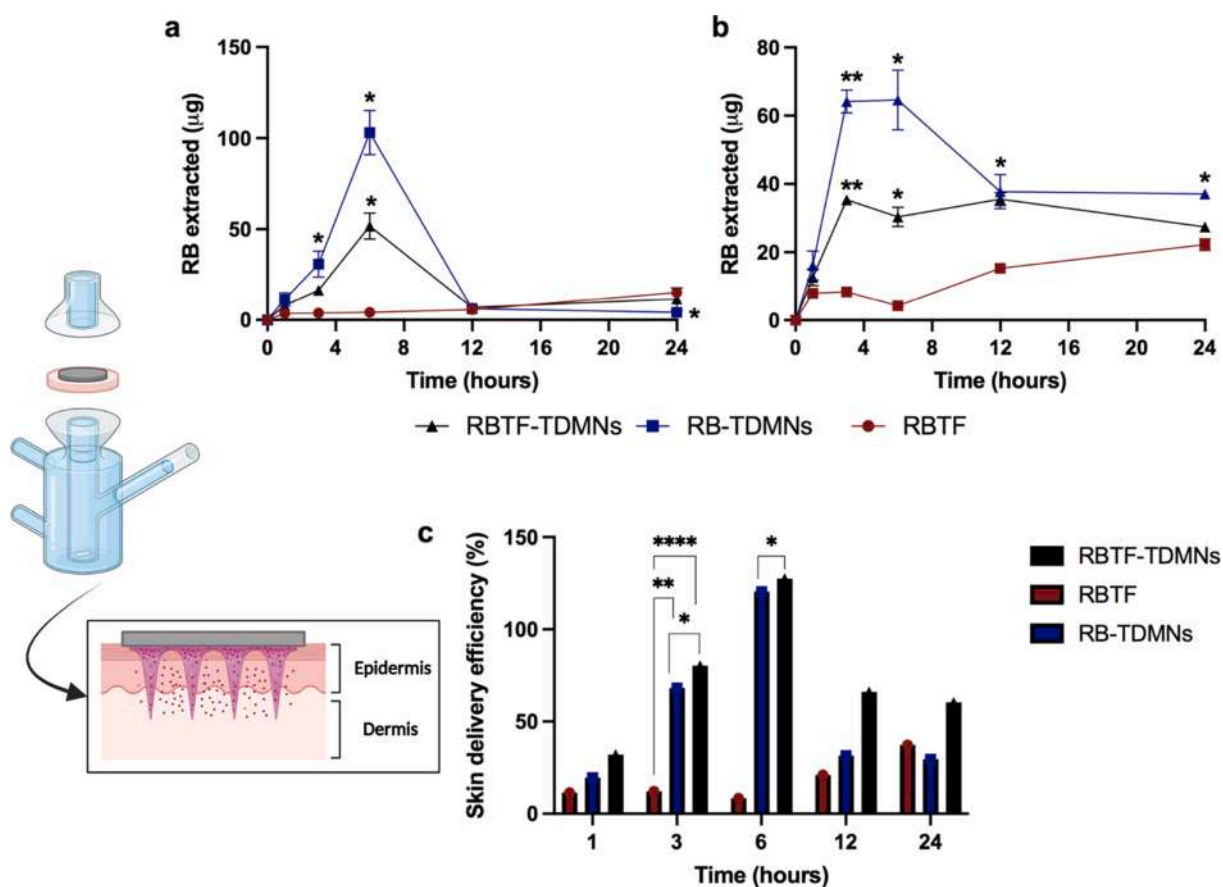

Fig. 9. *Ex-vivo* dermatokinetic study. Amount of RB extracted from (a) epidermis and (b) dermis of excised neonatal porcine skin. (c) The delivery efficiency of RB delivered into the skin over 24 h (values represent means ± SEM, n = 3). **** p value < 0.0001; ** p value < 0.01; * p value < 0.5.

the patient in terms of the quality of life. Melanoma at early stages (0, I and II) extends through the epidermis and further into the dermis in case of disease at stage II. Thus, in the dermatokinetic study, we focused on the RB amount accumulated in the epidermis (SC and viable epidermis) and dermis following the application of the formulations to the skin's outer surface, using a Franz diffusion cell set-up. Franz cells are widely used to study the percutaneous absorption of topically applied drugs, and several studies in the literature have highlighted their value in analysing dermal drug delivery (Moolakkadath et al., 2018; Raza et al., 2013; Zhang and Michniak-Kohn, 2018). Furthermore, Franz cells have been used to assess the drug delivery utilising *ex-vivo* skin of varying thickness as a diffusional barrier (Ameri et al., 2018). Herein, we chose porcine skin as a model diffusional barrier due to its similar morphology and function to its human counterpart; notably, we employed full-thickness porcine skin instead of dermatomed to prevent any alteration of the skin biomechanical properties, which may cause an over-penetration of TDMNs into the skin (Essaghraoui et al., 2019; Sabri et al., 2020). The RB amount delivered in the porcine's skin epidermis and dermis and the corresponding delivery efficiencies are depicted in Fig. 9.

The skin treated with RBTF dispersion delivered a significantly lower RB amount than both the TDMNs formulations, clearly demonstrating the value of TDMNs as an epidermal and dermal delivery system. The application of RBTF dispersion onto the skin's surface implies that the vesicles migrate through the different layers of the tissue to reach the target site; the presence of the surfactant in the formulation of RBTF makes the vesicles flexible and able to withstand this process. Even though TF show better performances than liposomes, the predecessors, the permeation mechanism is still controversial in the literature. TF are supposed to squeeze and pass-through skin pores without losing their integrity; however, other processes are also contemplated, including the structural modification of the intracellular lipid matrix and the vesicle's adsorption to and fusion with the SC (Cevc and Blume, 1992; El Maghraby et al., 2010). Therefore, part of the RBTF may lose its main structural characteristics during the permeation process or leak, causing undesired drug waste and reducing the APIs delivered to the dermis. Moreover, formulating RB in TF is critical to improving cellular uptake and therapeutic efficiency; thus, the delivery at the target site of intact RBTF is crucial in this project. On the opposite, as shown in section 3.5, both the TDMNs penetrated the skin to a depth of around 400 μm, thus physically allowing the encapsulated cargo to reach the target site, circumventing the migration process limits. Moreover, as anticipated in section 3.3, the current TDMNs are equipped with a solid PLA baseplate in contact with the skin surface that provides an occlusive dressing minimising the transepidermal water loss and contributing to the drug permeation through the tissue (Barry, 2001; Björklund et al., 2010).

Once experimentally proved the role of the trilayer dissolving MNs technology in cutaneous drug delivery, we evaluated the different RB permeation profiles from the RB-TDMNs and RBTF-TDMNs. RB-TDMNs showed a similar profile of intradermal delivery capability as RBTF-TDMNs but provided a faster permeation. During the first 6 h, the RB permeation from RB-TDMNs was significantly higher than RBTF-TDMNs into both epidermis (p value < 0.05) and dermis layers (p value < 0.05). However, regarding skin delivery efficiency, RBTF-TDMNs deposited an RB amount higher than RB-TDMNs into the skin strata at 6 h. The results suggest that the inclusion of RBTF into RBTF-TDMNs allowed a higher deposition and better-equilibrated distribution of the drug cargo within the epidermis and dermis compared to RB-TDMNs, improving the delivery efficiency and avoiding drug waste. The dermal delivery profile further suggests that the inclusion of RBTF in the polymer matrix increased the residence time of RB into the dermis compared to RB-TDMNs. Indeed, it is essential to highlight a dramatic decrease in RB percentage delivery from 12 h to 24 h. This is possibly due to RB permeation across the skin and into the receptor compartment increasing over the dermatokinetic studies.

The findings reported above may be explained considering the physical–chemical profile of the RB molecule. RB disodium salt is highly water-soluble (100 g/L) and amphiphilic (log P=0.59), with a significant tendency for hydrophilicity. TDMNs rapidly dissolved in the water-rich skin surrounding (section 3.6), releasing the encapsulated cargo. It is likely that free RB, once bypassed the SC barrier thanks to RB-TDMNs, has quickly migrated to the deepest skin layers containing more water than the upper ones due to the skin hydration gradient (Björklund et al., 2010). Nevertheless, the encapsulation of RB in TF enhances its hydrophobicity (Ali, 2011) and consequently the affinity for lipid-rich environments, thus slowing the permeation rate from the epidermis to the dermis and increasing the overall RB residence time in the skin layers. This hypothesis is supported by analysing the skin permeation profiles of water-soluble and hydrophobic drugs released by analogues dissolving MNs. Recently, the drug delivery efficiency of the same dissolving MNs containing, in one case, ibuprofen sodium (water-soluble) and, in the second case, itraconazole (hydrophobic) was compared (Anjani et al., 2022). The study demonstrated the higher permeation of ibuprofen sodium across the skin compared to itraconazole, which instead deposited into the skin. Similarly, the authors attributed the poor skin permeation of itraconazole to its low aqueous solubility.

To conclude, the dermatokinetic study showed that formulating RB in RBTF-TDMNs was an effective strategy to improve drug delivery to the skin layers affected by early-stage melanoma. As already stated, it is essential to remind that RBTF is also fundamental to promoting the interaction of RB with melanoma cancer cells, as proved in our previous research work (Demartis et al., 2021b).

4. Conclusion

The current work aimed to investigate the ability of TDMNs to act as an RB-loaded TF intradermal delivery system as an adjuvant tool in early-stage melanoma surgical management. TDMNs can play an essential role in avoiding a late recurrence of the disease, as they painlessly pierce the skin releasing the active cargo directly to the target site. We demonstrated that the novel RBTF-TDMNs were strong enough to penetrate the skin. They rapidly dissolved in the tissue fluid to release RBTF, which were successfully deposited in the area affected by melanoma at an early stage. Notably, RBTF-TDMNS significantly increased the amount of RB deposited in the skin compared to the RBTF dispersion; more importantly, the delivery efficiency of RBTF-TDMNs was higher than the TDMNs loaded with the free drug. The integration into the polymer matrix and the release process did not alter the RBTF structural characteristics essential to preserving the advantages of nanotechnology. The outcomes of this research strongly encourage considering RBTF-TDMNs a valuable tool to fight melanoma cancer. Even if this investigation is focused on intradermal delivery, *in vivo* testing would be of great value to better understand a realistic condition. To the best of our knowledge, the pharmacokinetics of RB, alone and when associated with lipid carriers, are not deeply documented in the literature, and it's necessary to go through this topic since it is highly employed in the biomedical field, specifically in cancer therapy. In this regard, it is our goal to elucidate the *in vivo* behaviour of pure RB, RBTF and RBTF-TDMNs in future investigations.

CRediT authorship contribution statement

Sara Demartis: Conceptualization, Investigation, Validation, Formal analysis, Writing – original draft, Visualization. **Qonita Kurnia Anjani:** Methodology, Validation, Formal analysis, Investigation, Writing – review & editing. **Fabiana Volpe-Zanutto:** Methodology, Investigation, Writing – review & editing. **Alejandro J. Paredes:**

Conceptualization, Writing – review & editing. **Subrin A. Jahan:** Investigation. **Lalitkumar K. Vora:** Writing – review & editing. **Ryan F. Donnelly:** Conceptualization, Resources, Writing – review & editing, Supervision. **Elisabetta Gavini:** Conceptualization, Writing – review & editing, Supervision.

Declaration of Competing Interest

The authors declare that they have no known competing financial interests or personal relationships that could have appeared to influence the work reported in this paper.

Acknowledgements

Appendix A. Supplementary material

Supplementary data to this article can be found online at https://doi.org/10.1016/j.ijpharm.2022.122217.

References

Aldawood, F.K., Andar, A., Desai, S., 2021. A comprehensive review of microneedles: types, materials, processes, characterizations and applications. Polymers 13, 2815. https://doi.org/10.3390/polym13162815.

Ali, M.F.M., 2011. Topical delivery and photodynamic evaluation of a multivesicular liposomal Rose Bengal. Lasers Med. Sci. 26, 267–275.

Ameri, M., Lewis, H., Lehman, P., 2018. Effect of skin model on *in vitro* performance of an adhesive dermally applied microarray coated with Zolmitriptan. J. Pharm. 2018, 1–5. https://doi.org/10.1155/2018/7459124.

Anjani, Q.K., Sabri, A.H.B., Utomo, E., Domínguez-Robles, J., Donnelly, R.F., 2022. Elucidating the impact of surfactants on the performance of dissolving microneedle array patches. Mol. Pharmaceutics 19, 1191–1208. https://doi.org/10.1021/acs.molpharmaceut.1c00988.

Barba, A.A., Bochicchio, S., Lamberti, G., Dalmoro, A., 2014. Ultrasonic energy in liposome production: process modelling and size calculation. Soft Matter 10, 2574. https://doi.org/10.1039/c3sm52879k.

Barry, B.W., 2001. Novel mechanisms and devices to enable successful transdermal drug delivery. Eur. J. Pharm. Sci. 14, 101–114. https://doi.org/10.1016/S0928-0987(01)00167-1.

Bhadale, R.S., Londhe, V.Y., 2022. Inclusion complexed iloperidone loaded dissolving microneedles: Characterization, in-vitro study, and dermatopharmacokinetics. J. Drug Delivery Sci. Technol. 68, 103063 https://doi.org/10.1016/j.jddst.2021.103063.

Björklund, S., Engblom, J., Thuresson, K., Sparr, E., 2010. A water gradient can be used to regulate drug transport across skin. J. Control. Release 143, 191–200. https://doi.org/10.1016/j.jconrel.2010.01.005.

Bloksgaard, M., Brewer, J., Bagatolli, L.A., 2013. Structural and dynamical aspects of skin studied by multiphoton excitation fluorescence microscopy-based methods. Eur. J. Pharm. Sci. 50, 586–594. https://doi.org/10.1016/j.ejps.2013.04.010.

Cevc, G., Blume, G., 1992. Lipid vesicles penetrate into intact skin owing to the transdermal osmotic gradients and hydration force. Biochim. Biophys. Acta (BBA) - Biomembranes 1104, 226–232, doi: 10.1016/0005-2736(92)90154-E.

Chang, C.-C., Yang, Y.-T., Yang, J.-C., Wu, H.-D., Tsai, T., 2008. Absorption and emission spectral shifts of rose bengal associated with DMPC liposomes. Dyes Pigm. 79, 170–175. https://doi.org/10.1016/j.dyepig.2008.02.003.

Cullen, J.K., Simmons, J.L., Parsons, P.G., Boyle, G.M., 2020. Topical treatments for skin cancer. Adv. Drug Deliv. Rev. 153, 54–64. https://doi.org/10.1016/j.addr.2019.11.002.

Demartis, S., Obinu, A., Gavini, E., Giunchedi, P., Rassu, G., 2021a. Nanotechnology-based rose Bengal: a broad-spectrum biomedical tool. Dyes Pigm. 188, 109236 https://doi.org/10.1016/j.dyepig.2021.109236.

Demartis, S., Rassu, G., Murgia, S., Casula, L., Giunchedi, P., Gavini, E., 2021. Improving dermal delivery of rose Bengal by deformable lipid nanovesicles for topical treatment of melanoma. Mol. Pharm. acs.molpharmaceut.1c00468. doi: 10.1021/acs.molpharmaceut.1c00468.

Domingues, B., Lopes, J., Soares, P., Populo, H., 2018. Melanoma treatment in review. ITT 7, 35–49. https://doi.org/10.2147/ITT.S134842.

El Maghraby, G.M.M., Williams, A.C., Barry, B.W., 2010. Can drug-bearing liposomes penetrate intact skin? J. Pharm. Pharmacol. 58, 415–429. https://doi.org/10.1211/jpp.58.4.0001.

El-Bashir, S.M., Yahia, I.S., Binhussain, M.A., AlSalhi, M.S., 2017. Designing of PVA/Rose Bengal long-pass optical window applications. Results Phys. 7, 1238–1244. https://doi.org/10.1016/j.rinp.2017.03.033.

Essaghraoui, A., Belfkira, A., Hamdaoui, B., Nunes, C., Lima, S.A.C., Reis, S., 2019. Improved dermal delivery of cyclosporine A loaded in solid lipid nanoparticles. Nanomaterials 9, 1204. https://doi.org/10.3390/nano9091204.

Hugo, E., Abuin, E., Lissi, E., Alarcón, E., Edwards, A.M., 2011. Effect of temperature on the photobehavior of Rose Bengal associated with dipalmitoylphosphatidyl choline liposomes. J. Lumin. 131, 2468–2472. https://doi.org/10.1016/j.jlumin.2011.06.021.

Ito, A., Watanabe, H., Naito, M., Aoyama, H., Nakagawa, Y., Fujimoto, N., 1986. Induction of thyroid tumors in (C57BL/6N x C3H/N)F1 mice by oral administration of 9–3',4',5',6'-tetrachloro-o-carboxy phenyl-6-hydroxy-2,4,5,7-tetraiodo-3-isoxanthone sodium (Food Red 105, rose bengal B). J. Natl. Cancer Inst. 77, 277–281.

Walters, K.A., Brain, K.R., 2002. Dermatological formulations and transdermal system. In: Dermatological and Transdermal Formulations. CRC Press, pp. 337–418.

Krishnan, V., Mitragotri, S., 2020. Nanoparticles for topical drug delivery: Potential for skin cancer treatment. Adv. Drug Deliv. Rev. 153, 87–108. https://doi.org/10.1016/j.addr.2020.05.011.

Lanza, J.S., Vucen, S., Flynn, O., Donadei, A., Cojean, S., Loiseau, P.M., Fernandes, A.P.S.M., Frézard, F., Moore, A.C., 2020. A TLR9-adjuvanted vaccine formulated into dissolvable microneedle patches or cationic liposomes protects against leishmaniasis after skin or subcutaneous immunization. Int. J. Pharm. 586, 119390 https://doi.org/10.1016/j.ijpharm.2020.119390.

Larrañeta, E., Moore, J., Vicente-Pérez, E.M., González-Vázquez, P., Lutton, R., Woolfson, A.D., Donnelly, R.F., 2014. A proposed model membrane and test method for microneedle insertion studies. Int. J. Pharm. 472, 65–73. https://doi.org/10.1016/j.ijpharm.2014.05.042.

Lee, E.-H., Lee, M.-K., Lim, S.-J., 2021. Enhanced stability of indocyanine green by encapsulation in zein-phosphatidylcholine hybrid nanoparticles for use in the phototherapy of cancer. Pharmaceutics 13, 305. https://doi.org/10.3390/pharmaceutics13030305.

Leonardi, G., Falzone, L., Salemi, R., Zanghï¿½, A., Spandidos, D., Mccubrey, J., Candido, S., Libra, M., 2018. Cutaneous melanoma: From pathogenesis to therapy (Review). Int. J. Oncol. doi: 10.3892/ijo.2018.4287.

Leonyza, A., Surini, S., 2019. Optimization of sodium deoxycholate-based transfersomes for percutaneous delivery of peptides and proteins. Int. J. App. Pharm., 329–332. doi: 10.22159/ijap.2019v11i5.33615.

Li, M., Vora, L.K., Peng, K., Donnelly, R.F., 2021. Trilayer microneedle array assisted transdermal and intradermal delivery of dexamethasone. Int. J. Pharm. 121295 https://doi.org/10.1016/j.ijpharm.2021.121295.

Li, Z., Fang, Y., Chen, H., Zhang, T., Yin, X., Man, J., Yang, X., Lu, M., 2022. Spatiotemporal trends of the global burden of melanoma in 204 countries and territories from 1990 to 2019: results from the 2019 global burden of disease study. Neoplasia 24, 12–21. https://doi.org/10.1016/j.neo.2021.11.013.

Lin, C.-M., Li, C.-S., Sheng, Y.-J., Wu, D.T., Tsao, H.-K., 2012. Size-dependent properties of small unilamellar vesicles formed by model lipids. Langmuir 28, 689–700. https://doi.org/10.1021/la203755v.

Liu, H., Innamarato, P.P., Kodumudi, K., Weber, A., Nemoto, S., Robinson, J.L., Crago, G., McCardle, T., Royster, E., Sarnaik, A.A., Pilon-Thomas, S., 2016. Intralesional rose bengal in melanoma elicits tumor immunity *via* activation of dendritic cells by the release of high mobility group box 1. Oncotarget 7, 37893–37905. https://doi.org/10.18632/oncotarget.9247.

McGuckin, M.B., Wang, J., Ghanma, R., Qin, N., Palma, S.D., Donnelly, R.F., Paredes, A. J., 2022. Nanocrystals as a master key to deliver hydrophobic drugs via multiple administration routes. J. Control. Release 345, 334–353. https://doi.org/10.1016/j.jconrel.2022.03.012.

Moolakkadath, T., Aqil, M., Ahad, A., Imam, S.S., Iqbal, B., Sultana, Y., Mujeeb, M., Iqbal, Z., 2018. Development of transethosomes formulation for dermal fisetin delivery: Box-Behnken design, optimization, *in vitro* skin penetration, vesicles–skin interaction and dermatokinetic studies. Artif. Cells Nanomed. Biotechnol. 46, 755–765. https://doi.org/10.1080/21691401.2018.1469025.

Mousavi, S., Hersey, P., 2007. Role of caspases and reactive oxygen species in rose bengal-induced toxicity in melanoma cells. Iran J. Basic Med. Sci. 10.

Mousavi, S.H., Dong, Z.X., Sharifi, A.M., Hersey, P., 2006. Study of rose bengal-induced cell death in melanoma cells in the absence of light. Iran. J. Basic Med. Sci. 9, 216–222.

Napolitano, S., Brancaccio, G., Argenziano, G., Martinelli, E., Morgillo, F., Ciardiello, F., Troiani, T., 2018. It is finally time for adjuvant therapy in melanoma. Cancer Treat. Rev. 69, 101–111. https://doi.org/10.1016/j.ctrv.2018.06.003.

Newcomer, K., Robbins, K.J., Perone, J., Hinojosa, F.L., Chen, D., Jones, S., Kaufman, C. K., Weiser, R., Fields, R.C., Tyler, D.S., 2022. Malignant melanoma: evolving practice management in an era of increasingly effective systemic therapies. Curr. Probl. Surg. 59, 101030 https://doi.org/10.1016/j.cpsurg.2021.101030.

Paredes, A.J., Volpe-Zanutto, F., Permana, A.D., Murphy, A.J., Picco, C.J., Vora, L.K., Coulter, J.A., Donnelly, R.F., 2021. Novel tip-loaded dissolving and implantable microneedle array patches for sustained release of finasteride. Int. J. Pharm. 606, 120885 https://doi.org/10.1016/j.ijpharm.2021.120885.

Permana, A.D., Anjani, Q.K., Sartini, Utomo, E., Volpe-Zanutto, F., Paredes, A.J., Evary, Y.M., Mardikasari, S.A., Pratama, Muh.R., Tuany, I.N., Donnelly, R.F., 2021. Selective delivery of silver nanoparticles for improved treatment of biofilm skin infection using bacteria-responsive microparticles loaded into dissolving microneedles. Mater. Sci. Eng. C 120, 111786. doi: 10.1016/j.msec.2020.111786.

Permana, A.D., Paredes, A.J., Volpe-Zanutto, F., Anjani, Q.K., Utomo, E., Donnelly, R.F., 2020. Dissolving microneedle-mediated dermal delivery of itraconazole nanocrystals

for improved treatment of cutaneous candidiasis. Eur. J. Pharm. Biopharm. 154, 50–61. https://doi.org/10.1016/j.ejpb.2020.06.025.

Portugal, I., Jain, S., Severino, P., Priefer, R., 2021. Micro- and nano-based transdermal delivery systems of photosensitizing drugs for the treatment of cutaneous malignancies. Pharmaceuticals 14, 772. https://doi.org/10.3390/ph14080772.

Ramalheiro, A., Paris, J.L., Silva, B.F.B., Pires, L.R., 2020. Rapidly dissolving microneedles for the delivery of cubosome-like liquid crystalline nanoparticles with sustained release of rapamycin. Int. J. Pharm. 591, 119942 https://doi.org/10.1016/j.ijpharm.2020.119942.

Ramöller, I., McAlister, E., Bogan, A., Cordeiro, A., Donnelly, R., 2020. Novel design approaches in the fabrication of polymeric microarray patches via micromoulding. Micromachines 11, 554. https://doi.org/10.3390/mi11060554.

Raza, K., Singh, B., Singla, S., Wadhwa, S., Garg, B., Chhibber, S., Katare, O.P., 2013. Nanocolloidal carriers of isotretinoin: antimicrobial activity against *Propionibacterium acnes* and dermatokinetic modeling. Mol. Pharmaceutics 10, 1958–1963. https://doi.org/10.1021/mp300722f.

Sabri, A., Ogilvie, J., McKenna, J., Segal, J., Scurr, D., Marlow, M., 2020. Intradermal delivery of an immunomodulator for basal cell carcinoma; expanding the mechanistic insight into solid microneedle-enhanced delivery of hydrophobic molecules. Mol. Pharmaceutics 17, 2925–2937. https://doi.org/10.1021/acs.molpharmaceut.0c00347.

Salwa, Chevala, N.T., Jitta, S.R., Marques, S.M., Vaz, V.M., Kumar, L., 2021. Polymeric microneedles for transdermal delivery of nanoparticles: frontiers of formulation, sterility and stability aspects. J. Drug Deliv. Sci. Technol. 65, 102711. doi: 10.1016/j.jddst.2021.102711.

Sandby-Møller, J., Poulsen, T., Wulf, H.C., 2003. Epidermal thickness at different body sites: relationship to age, gender, pigmentation, blood content, skin type and smoking habits. Acta Dermato-Venereologica 83, 410–413. https://doi.org/10.1080/00015550310015419.

Sharma, M., Mittapelly, N., Banala, V.T., Urandur, S., Gautam, S., Marwaha, D., Rai, N., Singh, N., Gupta, A., Mitra, K., Mishra, P.R., 2022. Amalgamated microneedle array bearing Ribociclib-loaded transfersomes eradicates breast cancer *via* CD44 targeting. Biomacromolecules 23, 661–675. https://doi.org/10.1021/acs.biomac.1c01076.

Srivastava, P.K., Thakkar, H.P., 2021. QbD-driven development of dissolving microneedle patch loaded with ultradeformable liposomes encapsulated Noopept: exploring a patient friendly, once-daily option to manage dementia. Eur. J. Pharm. Sci. 164, 105909 https://doi.org/10.1016/j.ejps.2021.105909.

Srivastava, P.K., Thakkar, H.P., 2020. Vinpocetine loaded ultradeformable liposomes as fast dissolving microneedle patch: tackling treatment challenges of dementia. Eur. J. Pharm. Biopharm. 156, 176–190. https://doi.org/10.1016/j.ejpb.2020.09.006.

Stracke, F., Weiss, B., Lehr, C.-M., König, K., Schaefer, U.F., Schneider, M., 2006. Multiphoton microscopy for the investigation of dermal penetration of nanoparticle-borne drugs. J. Invest. Dermatol. 126, 2224–2233. https://doi.org/10.1038/sj.jid.5700374.

Van Eerdenbrugh, B., Van den Mooter, G., Augustijns, P., 2008. Top-down production of drug nanocrystals: Nanosuspension stabilization, miniaturization and transformation into solid products. Int. J. Pharm. 364, 64–75. https://doi.org/10.1016/j.ijpharm.2008.07.023.

Vanerio, N., Stijnen, M., de Mol, B.A.J.M., Kock, L.M., 2019. Biomedical applications of photo- and sono-activated Rose Bengal: a review. Photobiomodulation Photomed. Laser Surgery 37, 383–394. https://doi.org/10.1089/photob.2018.4604.

Volpe-Zanutto, F., Ferreira, L.T., Permana, A.D., Kirkby, M., Paredes, A.J., Vora, L.K., P. Bonfanti, A., Charlie-Silva, I., Raposo, C., Figueiredo, M.C., Sousa, I.M.O., Brisibe, A., Costa, F.T.M., Donnelly, R.F., Foglio, M.A., 2021. Artemether and lumefantrine dissolving microneedle patches with improved pharmacokinetic performance and antimalarial efficacy in mice infected with Plasmodium yoelii. J. Controlled Release 333, 298–315. doi: 10.1016/j.jconrel.2021.03.036.

Wachter, E.A., Dees, C., Harkins, J., Fisher, W.G., Scott, T., 2002. Imaging photosensitizer distribution and pharmacology using multiphoton microscopy. In: Farkas, D.L., Leif, R.C. (Eds.), Presented at the International Symposium on Biomedical Optics, San Jose, CA, p. 112. doi: 10.1117/12.468334.

Xi, L., Lin, Z., Qiu, F., Chen, S., Li, P., Chen, X., Wang, Z., Zheng, Y., 2022. Enhanced uptake and anti-maturation effect of celastrol-loaded mannosylated liposomes on dendritic cells for psoriasis treatment. Acta Pharm. Sin. B 12, 339–352. https://doi.org/10.1016/j.apsb.2021.07.019.

Yang, D., Chen, M., Sun, Y., Jin, Y., Lu, C., Pan, X., Quan, G., Wu, C., 2021. Microneedle-mediated transdermal drug delivery for treating diverse skin diseases. Acta Biomater. 121, 119–133. https://doi.org/10.1016/j.actbio.2020.12.004.

Yang, H., Wu, X., Zhou, Z., Chen, X., Kong, M., 2019. Enhanced transdermal lymphatic delivery of doxorubicin via hyaluronic acid based transfersomes/microneedle complex for tumor metastasis therapy. Int. J. Biol. Macromol. 125, 9–16. https://doi.org/10.1016/j.ijbiomac.2018.11.230.

Zhang, J., Michniak-Kohn, B.B., 2018. Investigation of microemulsion and microemulsion gel formulations for dermal delivery of clotrimazole. Int. J. Pharm. 536, 345–352. https://doi.org/10.1016/j.ijpharm.2017.11.041.

Zhou, P., Chen, C., Yue, X., Zhang, J., Huang, C., Zhao, S., Wu, A., Li, X., Qu, Y., Zhang, C., 2021. Strategy for osteoarthritis therapy: improved the delivery of triptolide using liposome-loaded dissolving microneedle arrays. Int. J. Pharm. 609, 121211 https://doi.org/10.1016/j.ijpharm.2021.121211.

Zhou, Z., Pang, J., Wu, X., Wu, W., Chen, X., Kong, M., 2020. Reverse immune suppressive microenvironment in tumor draining lymph nodes to enhance anti-PD1 immunotherapy via nanovaccine complexed microneedle. Nano Res. 13, 1509–1518. https://doi.org/10.1007/s12274-020-2737-5.